ELSEVIER

Chemical Physics 267 (2001) 99–114

Chemical Physics

www.elsevier.nl/locate/chemphys

The role of microscopic and macroscopic coherence in laser control

Vadim V. Lozovoy [1], Bruna I. Grimberg, Igor Pastirk [2], Marcos Dantus *

Department of Chemistry, Center for Fundamental Materials Research, Michigan State University, East Lansing, MI 48824-1322, USA

Received 6 October 2000

Abstract

In this article, we discuss microscopic and macroscopic coherences resulting from multiple pulse excitation of molecular samples. The wave packet formalism is applied to describe the interference of wave packets within a single molecule (microscopic coherence) and the macroscopic interference between the polarizations resulting from optical responses of a single molecule or from different molecules (macroscopic coherence). Experimental virtual echo and stimulated photon echo measurements with noncollinear, degenerate femtosecond pulses are presented where both of these coherences are shown to control the observed dynamics. Theoretical simulations of the rovibronic dynamics observed experimentally on iodine vapor are presented. The role of these coherences in laser control of quantum dynamics is discussed.

1. Introduction

Most schemes for laser control of molecular dynamics involve a combination of two fundamental paradigms. The first is known as the pump–dump method [1,2] and the second, involving quantum interference is known as coherent control [3]. In the pump–dump method, the time between the two pulses is used to determine the point in space and time at which the excited state wave packet is transferred to the product state. Many femtosecond pump–probe experiments can be considered to be variations of the pump–dump method, for example Refs. [4–8]. The coherent control scheme involves interference between different excitation pathways. Coherent control can be used to create a wave packet in the excited state with specific phase-space distribution that avoids parasitic chemical channels through constructive and destructive interference [3].

It is important to note that interference can be a microscopic or macroscopic phenomenon. Microscopic interference can be defined as that which only involves wave packets within a single molecule and the nonlinear response involves a single Liouville pathway. [3] Macroscopic interference can occur (a) between polarizations corresponding to

* Corresponding author. Fax: +1-517-353-3023/1793.
E-mail address: dantus@msu.edu (M. Dantus).

[1] Permanent address: N.N. Semenov Institute of Chemical Physics, RAS, Moscow, Russian Federation.

[2] Affiliated with the Institute for Nuclear Sciences "VINCA", Belgrade, F.R. Yugoslavia.

[3] Liouville pathways are characterized by particular sequences of electric field interactions producing a nonlinear optical signal. In the context of this article, the Liouville pathways of concern are those leading to significant third-order polarization as described in Section 2. See also Ref. [16].

0301-0104/01/$ - see front matter
PII: S0301-0104(01)00219-1

different Liouville pathways of a single molecule, (b) from polarizations resulting from the same Liouville pathway of different molecules, or (c) from polarizations resulting from different molecular responses of different molecules [9–13]. The macroscopic coherence literature includes reports on mixtures [14–16], on pulse sequences to achieve mode suppression [17–22] and on interference between Liouville paths [23]. Macroscopic coherence effects have not been discussed in the context of coherent control of molecular dynamics, perhaps because they sometimes arise from coherence among different molecules. Here we present arguments for the potential usefulness of macroscopic interference for laser control.

The theory presented here is based primarily on a wave packet analysis of four-wave mixing (FWM), for stimulated photon echo (SPE) and virtual echo (VE) phenomena. The simulations include rotational, vibrational and electronic degrees of freedom and are found to be in excellent agreement with the experimental results showing clear manifestations of microscopic and macroscopic interference. In the conclusion, we discuss the role of microscopic and macroscopic coherence in other multiple pulse experiments such as pump–probe and in laser control of neat and mixed samples.

2. Theory

2.1. Formulation

In this section we discuss the main ideas that lead to the distinction between microscopic and macroscopic coherence. For this purpose, we calculate the polarization resulting from a multiple pulse excitation using the wave packet formulation. The experimental results discussed here involve noncollinear laser pulses, requiring the introduction of a coordinate that locates each molecule in space ($\boldsymbol{x}$). The internal molecular coordinate is denoted by ($\boldsymbol{r}$). The model assumes that the initial state is a linear superposition of eigenfunctions with random phase, a condition that is valid for most systems under thermodynamic equilibrium. The interactions with the external electric fields are assumed weak and treated as a first-order perturbation. The electric fields are resonant with the spectroscopic transition between two electronic states. Our analysis is restricted up to third-order effects.

Interaction with each electric field is described using the time-dependent matrix elements of the dipole operator $V_{eg}^{[n]}(\boldsymbol{x},t)=\langle e|\boldsymbol{\mu}\cdot\boldsymbol{E}^{[n]}(t)|g\rangle$, where e and g indicate excited and ground state vibrational levels respectively, $\hat{\mu}$ is the transition dipole moment operator, and the electric field of the nth pulse is given by $\boldsymbol{E}^{[n]}(\boldsymbol{x},t)=E_0^{[n]}(t)\mathrm{e}^{-\mathrm{i}(\omega_0 t-\mathbf{k}_n\boldsymbol{x})}+\text{c.c.}$ (where $E_0^{[n]}(t)$ is the amplitude of the laser field, ω_0 is the carrier frequency, $\mathbf{k}_n$ is the wave vector of the nth pulse). For each matrix element we write (using the rotation wave approximation)

$$V_{eg}^{[n]}=\frac{\boldsymbol{\mu}_{eg}}{\hbar}\mathrm{e}^{\mathrm{i}\mathbf{k}_n\boldsymbol{x}}\int_{-\infty}^{+\infty}\mathrm{d}t E_0^{[n]}(t)\exp\left(\mathrm{i}(\omega_{eg}-\omega_0)t\right)=\frac{1}{2}A_{eg}^{[n]}\mathrm{e}^{\mathrm{i}\mathbf{k}_n\boldsymbol{x}},\tag{1}$$

where ω_{eg} and $\boldsymbol{\mu}_{eg}$ are the frequency and dipole moment of the $e\leftarrow g$ transitions.

The zero-order set of wave functions in the ground state is a linear combination of vibrational eigenfunctions, $|g(\boldsymbol{r})\rangle$, with $\Psi^{(0)}(\boldsymbol{r},t)=\sum_g\times\mathrm{e}^{-\mathrm{i}\varepsilon_g(t-t_1)/\hbar}|g(\boldsymbol{r})\rangle$, where t_1 is defined as zero time and ε_g is the energy of gth ground state vibrational level. Excitation with the first pulse at $t=t_1$ creates on the excited electronic state first-order wave packets $\Psi^{(1)}(\boldsymbol{x},\boldsymbol{r},t;\mathbf{k}_1)$ proportional to the factor $\exp\left(\mathrm{i}\mathbf{k}_1\boldsymbol{x}-\mathrm{i}\omega_0(t-t_1)\right)$. After the second pulse is applied at time $t=t_2$, a new set of first-order wave packets $\Psi^{(1)}(\boldsymbol{x},\boldsymbol{r},t;\mathbf{k}_2)$ is excited from the ground state, while a second-order wave packet $\Psi^{(2)}(\boldsymbol{x},\boldsymbol{r},t;\mathbf{k}_1-\mathbf{k}_2)$ is de-excited back into the ground electronic state as a result of stimulated emission process. This wave packet has a phase factor $\exp\left(\mathrm{i}(\mathbf{k}_1-\mathbf{k}_2)\boldsymbol{x}-\mathrm{i}\omega_0(t_2-t_1)\right)$. The parameter $\mathbf{k}_1-\mathbf{k}_2$ describes time order of the interacting pulses defining the time–space dependence of the wave packets. After the third pulse is applied at $t=t_3$, a first-order wave packet $\Psi^{(1)}(\boldsymbol{x},\boldsymbol{r},t;\mathbf{k}_3)$ is generated into the excited state, two second-order wave packets $\Psi^{(2)}(\boldsymbol{x},\boldsymbol{r},t;\mathbf{k}_1-\mathbf{k}_3)$ and $\Psi^{(2)}(\boldsymbol{x},\boldsymbol{r},t;\mathbf{k}_2-\mathbf{k}_3)$ are de-excited into the ground state and a third-order wave packet,

$\Psi^{(3)}(\boldsymbol{x},\boldsymbol{r},t;\mathbf{k}_1-\mathbf{k}_2+\mathbf{k}_3)$, is generated in the excited state.

The signs of the wave vectors for multiple interactions is determined by the rotating wave approximation (RWA), for a system with two electronic levels, and play a major role in the classification of FWM processes vide infra. After three pulses, the total wave function of a single molecule is given by the sum of eight wave packets:

$$\begin{aligned}\Psi(\boldsymbol{x},\boldsymbol{r},t) &= \Psi^{(0)} \\ &\quad + \Psi^{(1)}(\mathbf{k}_1) + \Psi^{(1)}(\mathbf{k}_2) + \Psi^{(1)}(\mathbf{k}_3) \\ &\quad + \Psi^{(2)}(\mathbf{k}_1-\mathbf{k}_2) + \Psi^{(2)}(\mathbf{k}_1-\mathbf{k}_3) + \Psi^{(2)}(\mathbf{k}_2-\mathbf{k}_3) \\ &\quad + \Psi^{(3)}(\mathbf{k}_1-\mathbf{k}_2+\mathbf{k}_3). \end{aligned} \tag{2}$$

It is important to keep track of the wave vectors for each component when dealing with noncollinear laser pulses. [4] The phase-matching condition requires conservation of energy and momentum. For simplicity, we omitted the coordinates $\boldsymbol{x}$, $\boldsymbol{r}$, and t in the wave function's notation.

The polarization of medium $\boldsymbol{P}(\boldsymbol{x},t)$ results from the average of the dipole moment operator

$$\boldsymbol{P}(\boldsymbol{x},t) \propto \langle \Psi(\boldsymbol{x},\boldsymbol{r},t)|\boldsymbol{\mu}(\boldsymbol{r},t)|\Psi(\boldsymbol{x},\boldsymbol{r},t)\rangle, \tag{3}$$

leading to the expansion of the polarization in terms of the external electric field. The electric field generated by the gaseous medium after interaction with the three pulses, $\boldsymbol{E}^{[4]}(\boldsymbol{x},t)$, is proportional to the third-order polarization, $\boldsymbol{P}^{(3)}(\boldsymbol{x},t)$. This polarization contains 10 complex conjugate pairs that result from substitution of Eq. (2) into Eq. (3) and gathering third-order terms, see Table 1. The signal is proportional to the intensity of the emitted light, $I^{[4]}(\boldsymbol{x},t) \to I(\boldsymbol{x},t)$. The directions of the signal beams are listed in Table 1. For $-\mathbf{k}_1+\mathbf{k}_2+\mathbf{k}_3$ the Liouville pathways known as R_2 and R_3 (plus their c.c. R_6 and R_7) contribute to the signal [13]. This phenomenon is called stimulated photon echo. For $\mathbf{k}_1-\mathbf{k}_2+\mathbf{k}_3$ the Liouville pathways known as R_1 and R_4 (plus their c.c. R_5 and R_8) contribute to the signal. This phenomenon is called VE [23]. The third-order polarization for each phenomenon is the sum of the polarizations from different Liouville pathways, $P^{(3)}_{\mathrm{VE}} = P^{(3)}_1 + P^{(3)}_4$ and $P^{(3)}_{\mathrm{SPE}} = P^{(3)}_2 + P^{(3)}_3$. The interference between the electric fields resulting from these polarizations results in a macroscopic interference. In the case of collinear excitation when $\mathbf{k}_1 = \mathbf{k}_2$, VE and SPE polarizations interfere [23]. The rest of the processes listed in Table 1 do not emit signal in the detected phase-matching direction, and are not considered in this discussion.

The FWM signals result from all the terms given in Table 1. Notice that for calculating $\boldsymbol{P}^{(3)}$ we collect expressions where $|\Psi^{(1)}\rangle$ or $|\Psi^{(3)}\rangle$ overlap with $\langle\Psi^{(2)}|$ or $\langle\Psi^{(0)}|$ respectively. In particular if $\boldsymbol{P}^{(3)}$ is proportional to $\langle\Psi^{(0)}|\boldsymbol{\mu}|\Psi^{(3)}\rangle$ or $\langle\Psi^{(2)}|\boldsymbol{\mu}|\Psi^{(1)}\rangle$. We can obtain information about the wave packet dynamics of the system by calculating the third-order polarization that is proportional to the average dipole moment operator between the even-order *bra* wave functions and odd-order *ket* wave functions. Naturally, the molecule does not know where transitions take place or whether the wave packet is on the bra or ket side, because it is not a molecular characteristic. The difference between bra and ket appears when we calculate any physical measurable value quantum mechanically averaging the corresponding operator. The separation of bra and ket interactions and collection of terms based on the phase matching direction reduces the calculation from 20 integrals (including complex conjugates) to four. The separation of bra and ket interactions is the foundation for the density matrix approach to nonlinear optics and powerful diagrammatic representations known as double-sided Feynman diagrams and ladder diagrams [13,24–26]. In this article, we use the wave packet presentation to illustrate the related dynamics initiated and measured with the three-pulse FWM. A density matrix based description of related experiments including double-sided Feynman diagrams and Liouville equation has been given in Refs. [27–29]. The ladder diagrams for the

[4] Terms $\Psi^{(2)}(\mathbf{k}_n-\mathbf{k}_n)$ and $\Psi^{(3)}(\mathbf{k}_n-\mathbf{k}_n+\mathbf{k}_n)$ are not included in Eq. (2) because they do not contribute to the FWM signal in the phase-matching direction. Such terms may contribute to fifth, seventh and higher odd-order polarizations not considered in this theoretical model explicitly.

Table 1
Third-order polarization components[a]

$\boldsymbol{P}^{(3)}$	Space–time modulation	Phenomena	Process
$\langle\Psi^{(2)}(\mathbf{k}_2-\mathbf{k}_3)\lvert\boldsymbol{\mu}\rvert\Psi^{(1)}(\mathbf{k}_1)\rangle+\text{c.c.}$	$\exp[\mathrm{i}(\mathbf{k}_1-\mathbf{k}_2+\mathbf{k}_3)\boldsymbol{x}-\mathrm{i}\omega_0 t]+\text{c.c.}$	VE	R_1+R_5
$\langle\Psi^{(2)}(\mathbf{k}_1-\mathbf{k}_3)\lvert\boldsymbol{\mu}\rvert\Psi^{(1)}(\mathbf{k}_1)\rangle+\text{c.c.}$	$\exp[\mathrm{i}\mathbf{k}_3\boldsymbol{x}-\mathrm{i}\omega_0 t]+\text{c.c.}$		
$\langle\Psi^{(2)}(\mathbf{k}_1-\mathbf{k}_2)\lvert\boldsymbol{\mu}\rvert\Psi^{(1)}(\mathbf{k}_1)\rangle+\text{c.c.}$	$\exp[\mathrm{i}\mathbf{k}_2\boldsymbol{x}-\mathrm{i}\omega_0 t]+\text{c.c.}$		
$\langle\Psi^{(2)}(\mathbf{k}_1-\mathbf{k}_2)\lvert\boldsymbol{\mu}\rvert\Psi^{(1)}(\mathbf{k}_2)\rangle+\text{c.c.}$	$\exp[\mathrm{i}(-\mathbf{k}_1+2\mathbf{k}_2)\boldsymbol{x}-\mathrm{i}\omega_0 t]+\text{c.c.}$		
$\langle\Psi^{(2)}(\mathbf{k}_1-\mathbf{k}_3)\lvert\boldsymbol{\mu}\rvert\Psi^{(1)}(\mathbf{k}_2)\rangle+\text{c.c.}$	$\exp[\mathrm{i}(-\mathbf{k}_1+\mathbf{k}_2+\mathbf{k}_3)\boldsymbol{x}-\mathrm{i}\omega_0 t]+\text{c.c.}$	SPE	R_2+R_6
$\langle\Psi^{(2)}(\mathbf{k}_2-\mathbf{k}_3)\lvert\boldsymbol{\mu}\rvert\Psi^{(1)}(\mathbf{k}_2)\rangle+\text{c.c.}$	$\exp[\mathrm{i}\mathbf{k}_3\boldsymbol{x}-\mathrm{i}\omega_0 t]+\text{c.c.}$		
$\langle\Psi^{(2)}(\mathbf{k}_1-\mathbf{k}_2)\lvert\boldsymbol{\mu}\rvert\Psi^{(1)}(\mathbf{k}_3)\rangle+\text{c.c.}$	$\exp[\mathrm{i}(-\mathbf{k}_1+\mathbf{k}_2+\mathbf{k}_3)\boldsymbol{x}-\mathrm{i}\omega_0 t]+\text{c.c.}$	SPE	R_3+R_7
$\langle\Psi^{(2)}(\mathbf{k}_1-\mathbf{k}_3)\lvert\boldsymbol{\mu}\rvert\Psi^{(1)}(\mathbf{k}_3)\rangle+\text{c.c.}$	$\exp[\mathrm{i}(-\mathbf{k}_1+2\mathbf{k}_3)\boldsymbol{x}-\mathrm{i}\omega_0 t]+\text{c.c.}$		
$\langle\Psi^{(2)}(\mathbf{k}_2-\mathbf{k}_3)\lvert\boldsymbol{\mu}\rvert\Psi^{(1)}(\mathbf{k}_3)\rangle+\text{c.c.}$	$\exp[\mathrm{i}(-\mathbf{k}_2+2\mathbf{k}_3)\boldsymbol{x}-\mathrm{i}\omega_0 t]+\text{c.c.}$		
$\langle\Psi^{(0)}\lvert\boldsymbol{\mu}\rvert\Psi^{(3)}(\mathbf{k}_1-\mathbf{k}_2+\mathbf{k}_3)\rangle+\text{c.c.}$	$\exp[\mathrm{i}(\mathbf{k}_1-\mathbf{k}_2+\mathbf{k}_3)\boldsymbol{x}-\mathrm{i}\omega_0 t]+\text{c.c.}$	VE	R_4+R_8

[a] The first column contains all terms that contribute to the third-order polarization $\boldsymbol{P}^{(3)}$ after interaction with three degenerate, time-separated, noncollinear laser pulses. The second column contains the space–time modulations for each term, which define the direction of the emitted light. In the last column, we indicate the response functions that contribute to the SPE and VE signals with phase matching condition $-\mathbf{k}_1+\mathbf{k}_2+\mathbf{k}_3$ and $\mathbf{k}_1-\mathbf{k}_2+\mathbf{k}_3$ respectively.

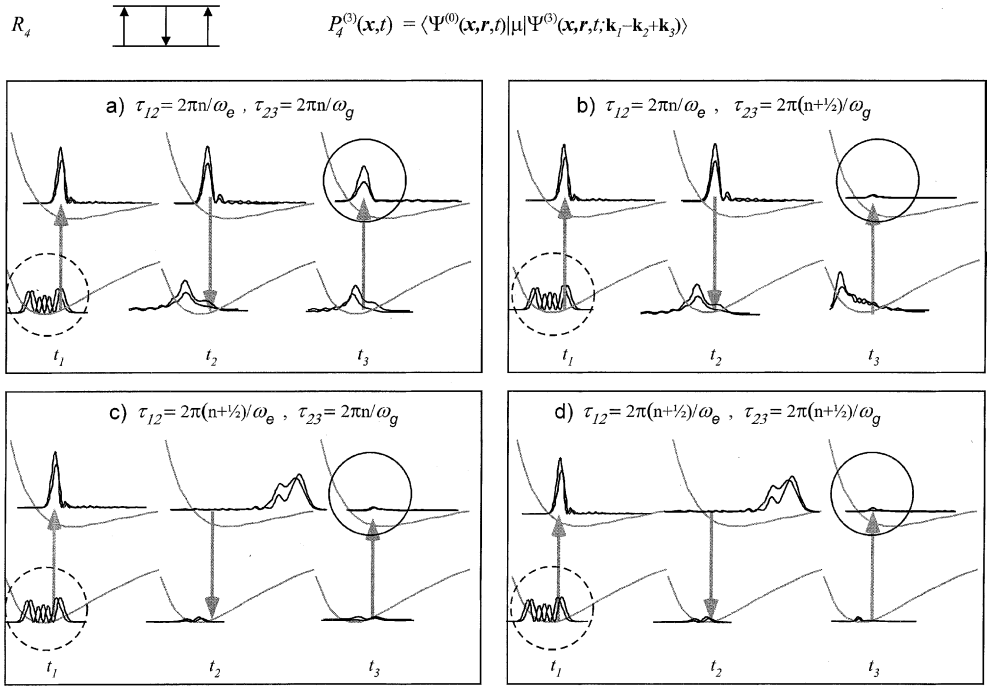

Fig. 1. Calculated wave packet snapshot of the R_4 nonlinear optical response due to the time–space dependent dipole matrix element $\langle\Psi^{(0)}\lvert\boldsymbol{\mu}\rvert\Psi^{(3)}(\mathbf{k}_1-\mathbf{k}_2+\mathbf{k}_3)\rangle+\text{c.c.}$ For this calculation equally populated $v''=2$ and 3 vibrational levels are considered, therefore, two wave packets appear after each interaction. The wave packets that contribute to the signal are indicated by solid (ket) and dashed (bra) circles. All transitions take place on the ket side. (a) All transitions are synchronized with packet motion and the polarization is maximized. (b) The population in the ground state after the second pulse is maximized, but the third pulse is out of phase with ground state oscillations. (c) The third pulse is in phase with ground state oscillations, but the population in the ground state after the second pulse is minimized. (d) When all transitions are out of phase with the wave packet motion the polarization is minimized.

VE and SPE pathways are shown in the upper-left corner of Figs. 1–4. The horizontal lines correspond to the ground and excited states. The vertical arrows can be considered to be absorption

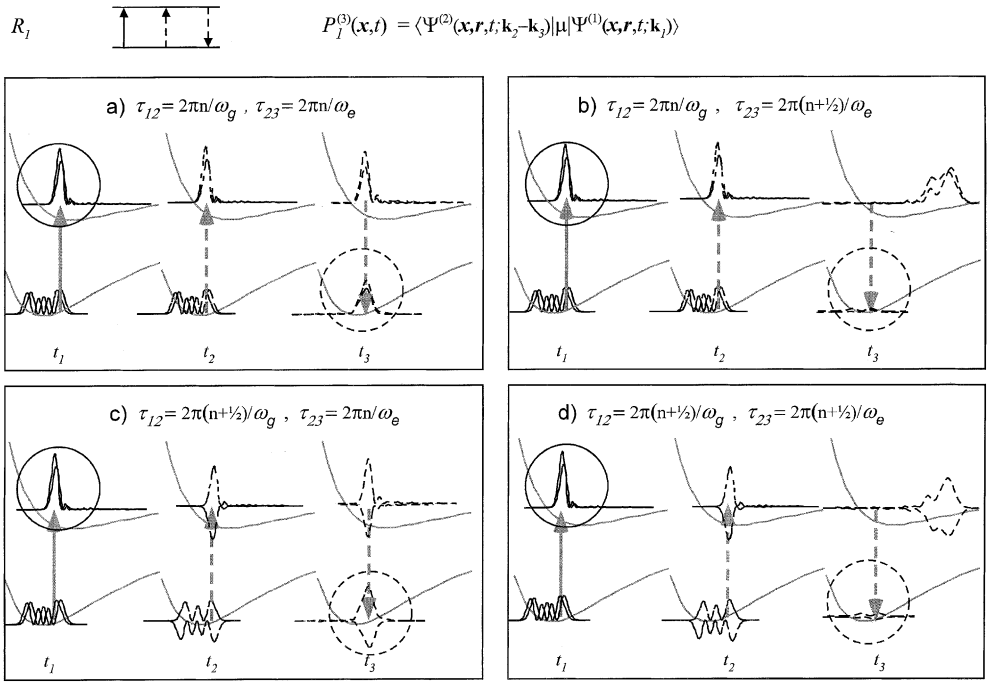

Fig. 2. Calculated wave packet snapshot of the R_1 nonlinear optical response due to the time–space dependent dipole matrix element $\langle \Psi^{(2)}(\mathbf{k}_2 - \mathbf{k}_3)|\boldsymbol{\mu}|\Psi^{(1)}(\mathbf{k}_1)\rangle + \text{c.c.}$ For this calculation equally populated $v'' = 2$ and 3 vibrational levels are considered, therefore, two wave packets appear after each interaction. The wave packets that contribute to the signal are indicated by solid (ket) and dashed (bra) circles. The transition on the ket at t_1 forms first-order wave packets $|\Psi^{(1)}(\mathbf{k}_1)\rangle$ and two transitions at t_2 and t_3 form second-order wave packets $\langle \Psi^{(2)}(\mathbf{k}_2 - \mathbf{k}_3)|$ on the bra side. (a) All transitions are synchronized with the wave packet motion and the polarization is maximized. (b) At t_2, the new bra excited state wave packets have the same phase and result in a constructive macroscopic interference. The third pulse is out of phase with the excited state oscillations. (c) At t_2 the two new bra excited state wave packets have opposite signs, resulting in a destructive macroscopic interference. The third pulse is in phase with excited state oscillations. (d) At t_2 the two new bra excited state wave packets have opposite signs, resulting in a destructive macroscopic interference. The third pulse is out of phase with the excited state oscillations.

(up) or stimulated emission (down). [5] Time goes from left to right. The solid lines correspond to $|\text{ket}\rangle$ interactions, while the dashed lines correspond to $\langle\text{bra}|$ interactions.

2.2. Wave packet dynamics

We have performed calculations of the wave packets discussed above using relevant spectroscopic parameters in order to visualize the dynamics involved and to identify the components that lead to the third-order polarization. The calculations of wave packet snapshots do not include rotations and are carried out with delta function pulses. Calculations with 60 fs pulses yielded similar results. The calculations assume equally populated $v'' = 2$ and 3 levels in the ground state and the excitation overlaps levels $v' = 6$–15 in the excited state and $v'' = 0$–6 in the ground state. The figures display the contribution of the absolute value squared of the wave function initiated from each vibrational state. Negative amplitude contributions represent destructive macroscopic interference.

The signal formation for the VE experiments depends on the Liouville pathways R_4 and R_1 (see Figs. 1 and 2). Both of these diagrams are

[5] Each arrow represents action with the photon annihilation or creation operator, absorption or emission, being physical observables, require two such interactions.

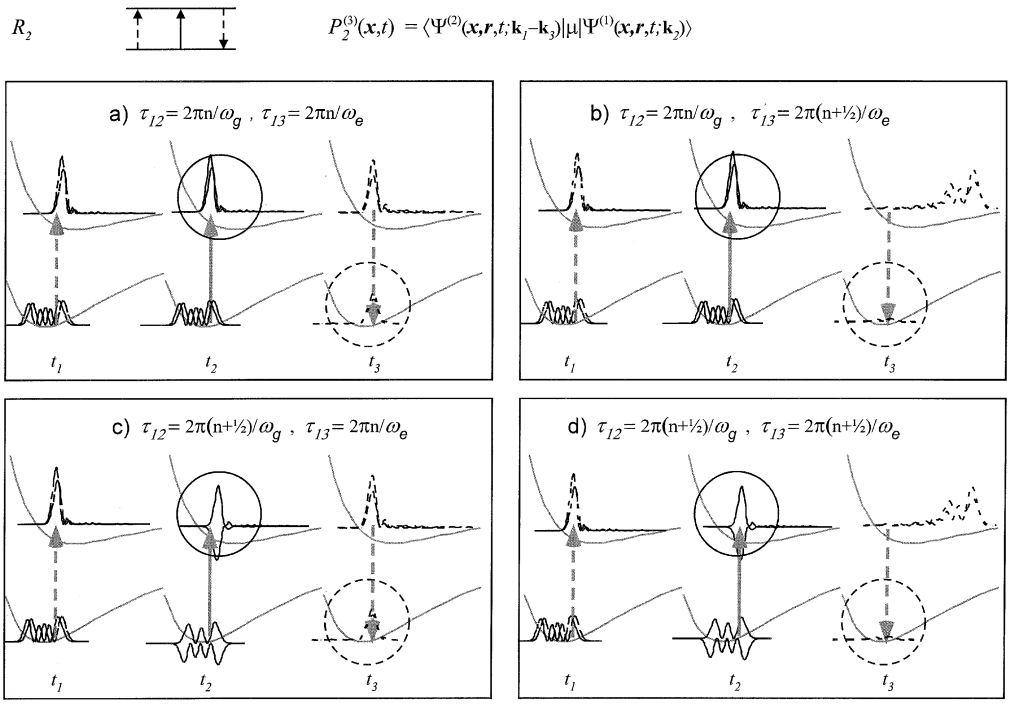

Fig. 3. Calculated wave packet snapshot of the R_2 nonlinear optical response due to the time–space dependent dipole matrix element $\langle \Psi^{(2)}(\mathbf{k}_1-\mathbf{k}_3)|\boldsymbol{\mu}|\Psi^{(1)}(\mathbf{k}_2)\rangle$ + c.c. For this calculation, equally populated $v''=2$ and 3 vibrational levels are considered, therefore, two wave packets appear after each interaction. The wave packets that contribute to the signal are indicated by solid (ket) and dashed (bra) circles. The transition on the ket at t_2 forms first-order wave packet $|\Psi^{(1)}(\mathbf{k}_2)\rangle$ and two transitions at t_1 and t_3 form second-order wave packet $\langle \Psi^{(2)}(\mathbf{k}_1-\mathbf{k}_3)|$ on the bra side. (a) All transitions are synchronized with the wave packet motion and the polarization is maximized. (b) At t_2, the new ket excited state wave packets have the same phase and results in a constructive macroscopic interference. The third pulse is out of phase with the excited sate oscillations. (c) At t_2 the two new ket excited state wave packets have opposite signs resulting in a destructive macroscopic interference. The third pulse is in phase with excited sate oscillations. (d) At t_2 the two new ket excited state wave packets have opposite signs, resulting in a destructive macroscopic interference. The third pulse is out of phase with the excited state oscillations.

initiated with a ket interaction. After the first two interactions, the system is in the ground state for R_4 and in the excited state for R_1. Wave packet snapshots for the R_4 Liouville pathways are presented in the Fig. 1. This pathway can be thought of as a pump–dump–pump sequence. The first pair of pulses creates a ground state wave packet. The amplitude of this packet is large when $\tau_{12} = 2\pi n/\omega_e$ (see Fig. 1a and b) or small when $\tau_{12} = 2\pi(n+0.5)/\omega_e$ (see Fig. 1c and d). The third pulse probes wave packet motion in the ground state. The amplitude of the signal is large when $\omega_g\tau_{23} = 2\pi n/\omega_g$ (see Fig. 1a and c) or small when $\tau_{23} = 2\pi(n+0.5)/\omega_g$ (see Fig. 1b and d). The largest contribution from the R_4 pathway is observed when $\tau_{12} = 2\pi n/\omega_e$ and $\tau_{23} = 2\pi n/\omega_g$. The third-order polarization for this pathway $P_4^{(3)}$ is proportional to the dipole coupling between the third-order wave packet in the excited state (solid circle) and the zeroth-order ground state wave functions (dashed circle) in Fig. 1.

Wave packet snapshots for the R_1 pathway are shown in the Fig. 2. The first pulse creates a first-order wave packet $\Psi^{(1)}(\mathbf{k}_1)$ on the excited state. The second pulse interacts with the ground state again and creates a second wave packet $\Psi^{(1)}(\mathbf{k}_2)$ on the excited PES. The third pulse dumps the wave packet created by the second pulse to form $\Psi^{(2)}(\mathbf{k}_2-\mathbf{k}_3)$. The signal results from the dipole coupling between the first wave packet, moving on the excited state (solid circle), and the wave packet moving on the ground state (dashed circle),

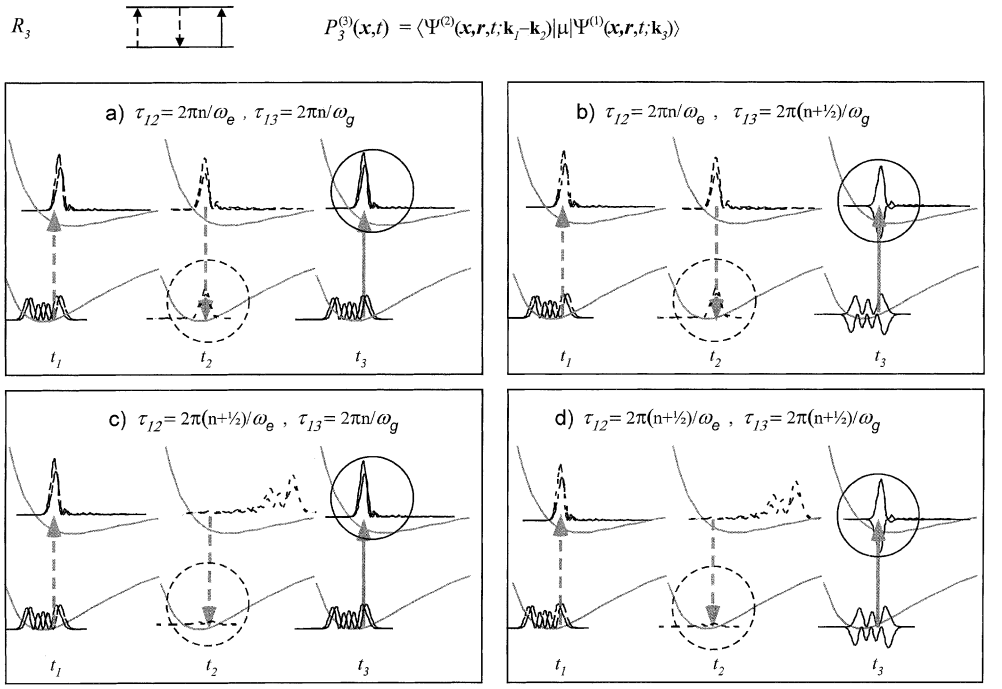

Fig. 4. Calculated wave packet snapshot of the R_3 nonlinear optical response due to the time–space dependent dipole matrix element $\langle \Psi^{(2)}(\mathbf{k}_1 - \mathbf{k}_2)|\boldsymbol{\mu}|\Psi^{(1)}(\mathbf{k}_3)\rangle + \text{c.c.}$ For this calculation, equally populated $v'' = 2$ and 3 vibrational levels are considered, therefore, two wave packets appear after each interaction. The wave packets that contribute to the signal are indicated by solid (ket) and dashed (bra) circles. Two transitions at t_1 and t_2 form second-order wave packets $\langle \Psi^{(2)}(\mathbf{k}_1 - \mathbf{k}_2)|$ on the bra side and the transition on the ket at t_3 forms first-order wave packets $|\Psi^{(1)}(\mathbf{k}_3)\rangle$. (a) All transitions are synchronized with the wave packet motion and the polarization is maximized. (b) The population in the ground state after the second pulse is maximized. The third pulse excites two new ket wave packets that have opposite signs, resulting in a destructive macroscopic interference. (c) The second pulse at t_2 is out of phase with the excited state dynamics. The third pulse excites two new ket wave packets resulting in a constructive macroscopic interference. (d) The second pulse at t_2 is out of phase with the excited state dynamics. The third pulse excites two new ket wave packets that have opposite signs resulting in a destructive macroscopic interference.

$\langle \Psi^{(2)}(\mathbf{k}_2 - \mathbf{k}_3)|\boldsymbol{\mu}|\Psi^{(1)}(\mathbf{k}_1)\rangle + \text{c.c.}$ The maximum signal from the R_1 pathway is observed when the third pulse is in phase with the wave packet motion on the excited state $\tau_{23} = 2\pi n/\omega_e$ (see Fig. 2a and c). R_1 is minimized when the last pulse is out of phase with respect to the excited state oscillation $\tau_{23} = 2\pi(n + 0.5)/\omega_e$ (see Fig. 2b and d). The signal from R_1 oscillates with the excited state vibrational frequency ω_e as a function of the scanned time delay τ_{23}.

The amplitude of the R_1 pathway has an additional dependence on the macroscopic interference between signals generated from wave packets excited from different initially populated vibrational levels in the ground state. Here we discuss this case with a model system having two equally populated vibrational levels in the ground state and multiple levels in the excited electronic state. The initial state of the system is a sum of two eigenstates $|n\rangle$, with random phases ϕ_n:

$$\Psi^{(0)}(t = 0) = \Psi_1^{(0)} + \Psi_2^{(0)} \equiv e^{i\phi_1}|1\rangle + e^{i\phi_2}|2\rangle. \quad (4)$$

After the first pulse the wave packet created in the excited state, is given by the sum of two first-order wave packets originating from the two ground state vibrational levels:

$$\Psi^{(1)}(\mathbf{k}_1) = \Psi_1^{(1)}(\mathbf{k}_1) + \Psi_2^{(1)}(\mathbf{k}_1). \quad (5)$$

It is important to realize that each wave packet is statistically independent because they are excited from different ground vibrational levels. After the

second pulse, a new wave packet is formed in the excited state, that is given by the sum of two first-order wave packets from different initial vibrational levels but now with a well-defined phase delay with respect to the wave packet in Eq. (4).

$$\Psi^{(1)}(\mathbf{k}_2) = \exp(-i\varepsilon_1\tau_{12}/\hbar)\Psi_1^{(1)}(\mathbf{k}_2) + \exp(-i\varepsilon_2\tau_{12}/\hbar)\Psi_2^{(1)}(\mathbf{k}_2). \quad (6)$$

After the third pulse, a second-order wave packet is formed in the ground state, and it is the sum of the two wave packets from Eq. (6).

$$\Psi^{(2)}(\mathbf{k}_2-\mathbf{k}_3) = \exp(-i\varepsilon_1\tau_{12}/\hbar)\Psi_1^{(2)}(\mathbf{k}_2-\mathbf{k}_3) + \exp(-i\varepsilon_2\tau_{12}/\hbar)\Psi_2^{(2)}(\mathbf{k}_2-\mathbf{k}_3). \quad (7)$$

The third-order polarization for R_1 is given by

$$P_1^{(3)} \propto \langle \exp(-i\varepsilon_1\tau_{12}/\hbar)\Psi_1^{(2)}(\mathbf{k}_2-\mathbf{k}_3) + \exp(-i\varepsilon_2\tau_{12}/\hbar)\Psi_2^{(2)}(\mathbf{k}_2-\mathbf{k}_3)| \times \boldsymbol{\mu}|\Psi_1^{(1)}(\mathbf{k}_1) + \Psi_2^{(1)}(\mathbf{k}_1)\rangle + \text{c.c.} \quad (8)$$

Because of the random phases between the initial eigenfunctions (see Eq. (4)) the cross terms in Eq. (8) are cancelled after the average over the phase, therefore the polarization is given by

$$P_1^{(3)} \propto \exp(-i\varepsilon_1\tau_{12}/\hbar)\langle\Psi_1^{(2)}(\mathbf{k}_2-\mathbf{k}_3)|\boldsymbol{\mu}|\Psi_1^{(1)}(\mathbf{k}_1)\rangle + \exp(-i\varepsilon_2\tau_{12}/\hbar)\langle\Psi_2^{(2)}(\mathbf{k}_2-\mathbf{k}_3)|\boldsymbol{\mu}|\Psi_2^{(1)}(\mathbf{k}_1)\rangle + \text{c.c.} \quad (9)$$

If the two wave packets in the excited state are sufficiently similar and the Frank–Condon approximation is valid then

$$\langle\Psi_1^{(2)}(\mathbf{k}_2-\mathbf{k}_3)|\boldsymbol{\mu}|\Psi_1^{(1)}(\mathbf{k}_1)\rangle \approx \langle\Psi_2^{(2)}(\mathbf{k}_2-\mathbf{k}_3)|\boldsymbol{\mu}|\Psi_2^{(1)}(\mathbf{k}_1)\rangle \approx \boldsymbol{\mu}\langle\Psi^{(2)}(\mathbf{k}_2-\mathbf{k}_3)|\Psi^{(1)}(\mathbf{k}_1)\rangle. \quad (10)$$

In this case, we can rewrite expression (9) as follows:

$$P_1^{(3)} \propto [\exp(-i\varepsilon_1\tau_{12}/\hbar) + \exp(-i\varepsilon_2\tau_{12}/\hbar)] \times \langle\Psi^{(2)}(\mathbf{k}_2-\mathbf{k}_3)|\Psi^{(1)}(\mathbf{k}_1)\rangle + \text{c.c.} \propto \cos(\tfrac{1}{2}\omega_g\tau_{12})\langle\Psi^{(2)}(\mathbf{k}_2-\mathbf{k}_3)|\Psi^{(1)}(\mathbf{k}_1)\rangle \quad (11)$$

and the signal from R_1 pathway is given by

$$I_1 \propto [1+\cos(\omega_g\tau_{12})]|\langle\Psi^{(2)}(\mathbf{k}_2-\mathbf{k}_3)|\Psi^{(1)}(\mathbf{k}_1)\rangle|^2. \quad (12)$$

The signal carries an oscillation with frequency ω_g as a function of τ_{12} that originates from the creation of two phase-related wave packets (see Eq. (6)). This oscillation leads to the observation of a macroscopic coherence.

This formal analytical result may be visualized with wave packet snapshots. When $\tau_{12} = 2\pi n/\omega_g$, the quantum phase difference between the excited state wave packets is zero or 2π (see Fig. 2a and b). When $\tau_{12} = 2\pi(n+0.5)/\omega_g$, the phase shift between the excited state wave packets is π, therefore, their amplitudes have opposite signs (see Fig. 2b and d). Because of this synchronization-interference sequence, the R_1 pathway's contribution to the signal can be maximized or minimized. This synchronization-interference control mechanism requires two or more initially populated ground states. When only one vibrational level is populated in the ground state this control 'knob' is lost.

Now we analyze the microscopic and macroscopic coherence in the SPE measurements. The analysis is analogous to that of the R_1 Liouville pathway but now performed for R_2 and R_3 (see Figs. 3 and 4, respectively). For both of these cases, the synchronization-interference mechanism plays a major role. Liouville pathways R_2 and R_3 contribute equally to the SPE signal (see the appendix and Figs. 3 and 4). The wave packet snapshots corresponding to the R_2 dynamics are shown in Fig. 3. The amplitude of this pathway depends on the timing between the wave packet motion on the excited state and the delay time between the first and third pulses. When $\tau_{13} = 2\pi n/\omega_e$, R_2 is maximized (see Fig. 3a and c) while for $\tau_{13} = 2\pi(n+\frac{1}{2})/\omega_e$, R_2 is minimized (see Fig. 3b and d). Both of these cases are due to pump–dump control. When $\tau_{12} = 2\pi n/\omega_g$ we have a maximum signal (see Fig. 3a and b) and when $\tau_{12} = 2\pi(n+\frac{1}{2})/\omega_g$, we have a minimum signal (see Fig. 3c and d). Both of these cases are due to synchronization interference. A similar analysis is valid for the R_3 process (see Fig. 4), however, the

pump–dump process occurs for τ_{12} and the synchronization interference occurs for τ_{13}.

A question that is usually raised for three-pulse FWM is why phase-locked pulses are not required with noncollinear beams. From a theoretical point of view, the electric field of different pulses may have a random phase θ_1, θ_2, θ_3. Each field is given by $\boldsymbol{E}^{[n]}(\boldsymbol{x},t) = E_0^{[n]}(t)\exp[-\mathrm{i}\omega_0 t + \mathrm{i}\mathbf{k}_n\boldsymbol{x} + \mathrm{i}\theta_n] + \text{c.c.}$ The system generates a new electric field $\boldsymbol{E}^{[4]}(\boldsymbol{x},t)$ that is proportional to $\exp[-\mathrm{i}\omega_0(t-(\mp t_1 \pm t_2 + t_3) + \mathrm{i}(\mp\mathbf{k}_1 \pm \mathbf{k}_2 + \mathbf{k}_3)\boldsymbol{x} + \mathrm{i}(\mp\theta_1 \pm \theta_2 + \theta_3)]$ (upper sign for SPE and lower sign for VE). In the case of homodyne detection, the phase dependence cancels after integration over time in the phase-matching direction $\mp(\mathbf{k}_1 - \mathbf{k}_2) + \mathbf{k}_3$. From a physical point of view, the grating formed after the first two pulses has a wave-vector $\mp(\mathbf{k}_1 - \mathbf{k}_2)$ and a random phase $\mp(\theta_1 - \theta_2)$. The third pulse diffracts from this grating in the direction $\mp(\mathbf{k}_1 - \mathbf{k}_2) + \mathbf{k}_3$ with phase $\mp(\theta_1 - \theta_2) + \theta_3$. This phase does not affect intensity measurements of the signal with time integrating detectors. For heterodyne detection, or other methods involving four interactions with the electric fields phase locking is required. For experiments using collinear pulses, the above distinctions do not apply and all processes in Table 1 interfere. A more detailed description of the theoretical parameters used for the calculation of electronic, vibrational and rotational degrees of freedom is included in the appendix.

3. Experimental

We have selected a simple molecular system and a powerful background-free detection method in order to explore coherent control with three-pulse sequences. The experiments were carried out on the $(\mathrm{B}^3\prod_{0+u} \leftrightarrow \mathrm{X}^1\Sigma_{0+g})$ transition of molecular iodine, for which the potential energy curves and spectroscopic constants are well known [30,31]. The experimental method is homodyne, spectrally integrated, noncollinear, femtosecond, three-pulse degenerate FWM [28,32–40]. The experiments were obtained with an amplified colliding-pulse mode-locked laser producing ~60 fs (FWHM) transform-limited Gaussian pulses which were then split into three time-delayed beams with an

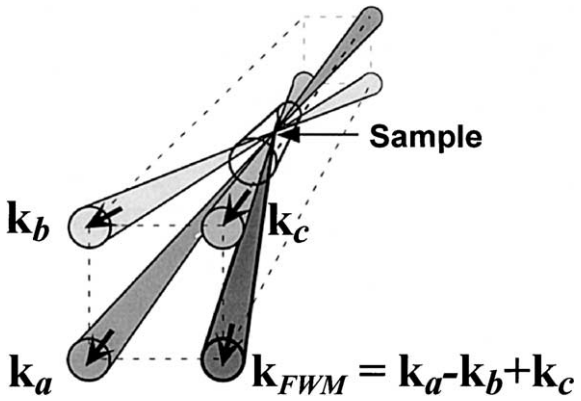

Fig. 5. Forward box configuration of the beams for the three-pulse FWM experiments. The three laser fields are applied in a given temporal sequence and overlapped spatially in the sample. The signal is detected in the direction of the wave vector $\mathbf{k}_{\mathrm{FWM}}$ that satisfies the phase-matching condition.

energy of approximately 30 μJ/pulse. The central wavelength of the pulses was 620 nm, which is resonant with the B–X transition in molecular iodine. Iodine was sealed in a quartz cell kept at 180°C. The optical density of the sample was 0.2, indicating a nonsaturated vapor pressure at this temperature. The laser pulses were arranged in a noncollinear geometry (see Fig. 5), and optimized for phase-matching detection [41,42]. The background-free FWM signal was collected in the direction $\mathbf{k}_{\mathrm{FWM}} = \mathbf{k}_{\mathrm{a}} - \mathbf{k}_{\mathrm{b}} + \mathbf{k}_{\mathrm{c}}$ with a 10 ns gated photomultiplier. We present two types of experiments SPE and VE. For both cases, pulse b defines time zero. Pulse a is fixed in time with respect to pulse b, while pulse c is scanned with an optical delay line. When pulse b is the first to reach the sample, the phase-matching condition is $\mathbf{k}_{\mathrm{SPE}} = -\mathbf{k}_1 + \mathbf{k}_2 + \mathbf{k}_3$ and hence an SPE signal is collected. This setup is often used to interrogate liquid samples [19,22]. If pulse b is the second to arrive at the sample, the phase-matching condition is $\mathbf{k}_{\mathrm{VE}} = \mathbf{k}_1 - \mathbf{k}_2 + \mathbf{k}_3$ and hence a VE signal is collected.

4. Results

The experimental results for the VE and SPE pulse sequences are presented in Figs. 6 and 7,

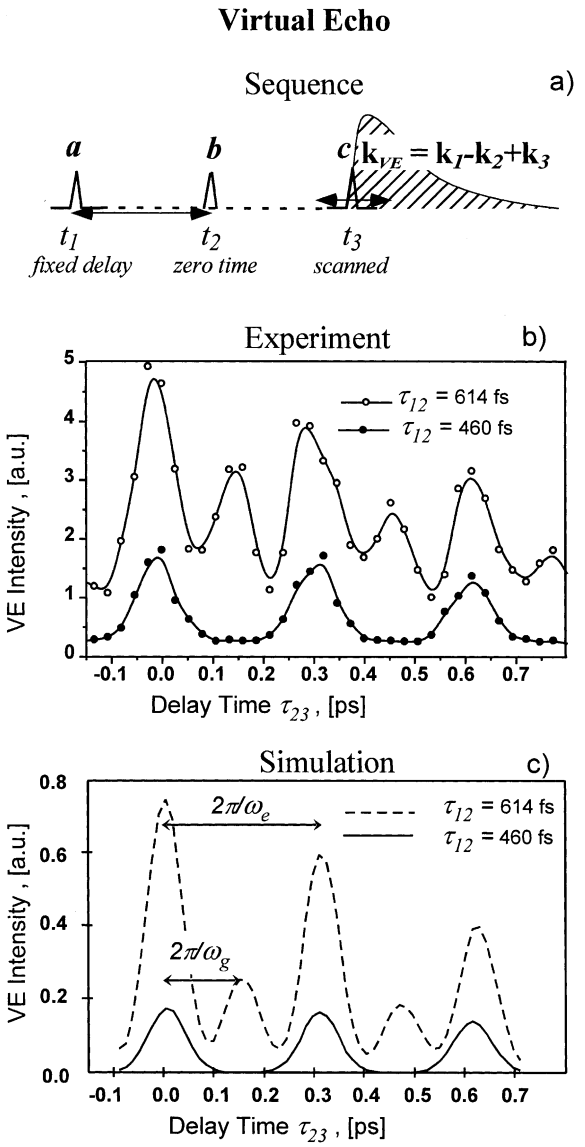

Fig. 6. (a) VE pulse sequence for the phase-matching condition $\mathbf{k}_{VE} = \mathbf{k}_1 - \mathbf{k}_2 + \mathbf{k}_3$. Pulse a is first, b is second and c is third. Pulse a has a fixed delay time with respect to b, the position of pulse b is defined as time zero, and pulse c scanned. (b) The experimental data, spectrally and time integrated, is shown for two delay times $\tau_{12} = 614$, 460 fs as a function of τ_{23}. When $\tau_{12} = 460$ fs, the oscillation period 307 fs of the VE signal corresponds to the vibrational motion of the excited state of I_2. When $\tau_{12} = 614$ fs, the additional oscillation with the ground state vibrational period of 160 fs appears. (c) Theoretical simulation of the VE signals.

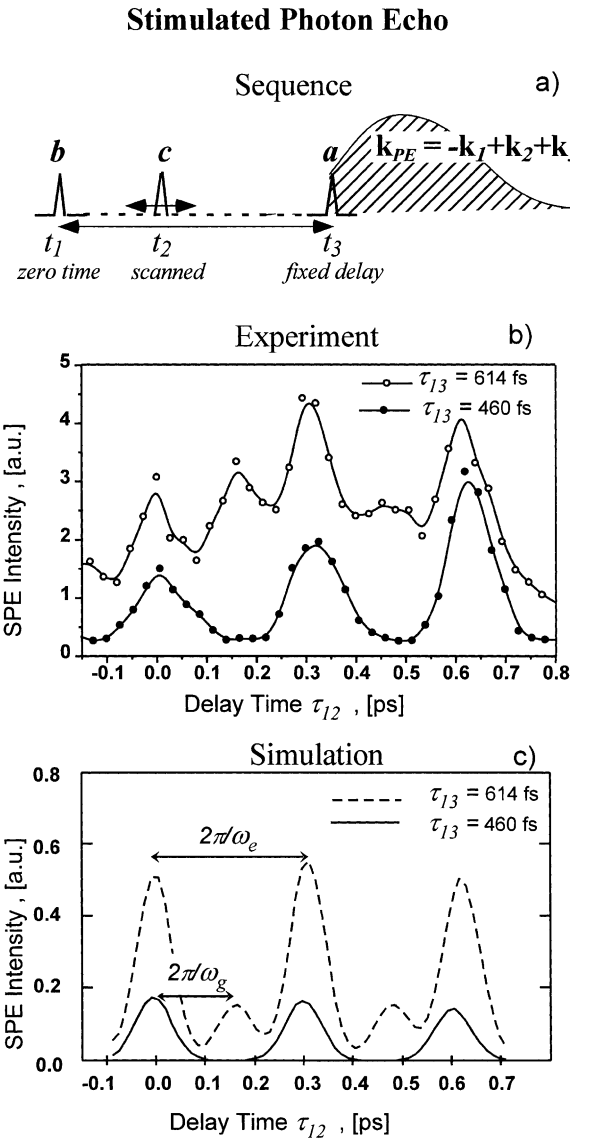

Fig. 7. (a) SPE pulse sequence for the phase-matching condition $\mathbf{k}_{VE} = -\mathbf{k}_1 + \mathbf{k}_2 + \mathbf{k}_3$. Pulse b is first, c is second and a is third. Pulse a has a fixed delay with respect to b, where the time of pulse b is defined as time zero, and pulse c is scanned. (b) The experimental data, spectrally and time integrated, is shown for two delay times $\tau_{13} = 614$, 460 fs and scanned τ_{12}. When $\tau_{13} = 460$ fs, the oscillation period (307 fs) of the SPE signal corresponds to the vibrational motion of the excited state molecules. When $\tau_{13} = 614$ fs, additional oscillations with the ground state vibrational period (160 fs) appears. (c) Theoretical simulation of the SPE signals.

respectively. The experimentally measured intensity of FWM emission intensity and modulation is similar for both experiments. Notice that when the delay time between the first two pulses equals 460 fs the VE data contains beats with a period of 307 fs. In a previous publication we showed long (15 ps) scans corresponding to a similar observation [43]. The Fourier transform of these data contains only one strong peak with maximum 108 cm^{-1}, corresponding to the classical vibrational frequency of the B state with vibrational quantum numbers $v' = 6$–11. When the delay between the first two pulses equals 614 fs the data contains the same excited state featuring together with additional peaks centered between two previous ones. The Fourier transform of a long scan for this condition contains a strong peak at 208 cm^{-1}. The temporal and spectral resolution is good enough to conclude that we are not observing the "second harmonic" of the excited state frequency, but rather the vibrational frequency in the ground electronic state with vibrational number $v'' = 2$–4, together with a contribution of the excited state.

The experimental observations of VE confirm the model discussed above. In Fig. 6b we see that when $\tau_{12} = 614$ fs the signal has ground state oscillations, but when $\tau_{12} = 460$ fs, the signal has no ground state contribution. This is a result of the R_4 pathway control. The contribution of the R_1 pathway is approximately two times smaller than that of R_4. This is because the three pulses are linearly polarized (see the appendix). The full quantum simulation of the signal (see Fig. 6c) using formulas from the appendix reproduces our experimental observations.

The experimental observations for SPE measurements shown in Fig. 7, support the theoretical approach discussed above. When $\tau_{13} = 614$ fs R_2 is maximized and when $\tau_{13} = 460$ fs it is minimized, due to the pump–probe mechanism. The R_2 pathway results in ground state oscillations as a function of τ_{12}. The situation is reversed for the R_3 pathway, namely, the dependence on τ_{12} gives an excited state oscillation. When $\tau_{13} = 460$ fs, the R_2 pathway is cancelled leaving only the excited state oscillations due to R_3. The theoretical simulations for the SPE data are based on the formulas in the appendix and are presented in Fig. 7c. The simulations shown were carried out with no adjustable parameters. Only rotational and vibrational spectroscopic parameters were included.

We call attention that despite the similarity between SPE and VE dynamics the source for the observed ground state oscillations is different. For the VE case it is the result of a microscopic interference, similar to the quantum beats observed in pump–probe or pump–dump processes, but for the SPE data the ground state oscillations result of macroscopic interference or synchronization interference caused by the coherence introduced by the pulses.

The ground and excited state dynamics observed with the VE method arise from the microscopic interference of wave packets in one Liouville pathway. Ground state dynamics results from wave packet motion in the ground state (R_4) while excited state dynamics from wave packet motion in the excited state (R_1). Similarly, the observation of the excited state dynamics in a SPE measurement results from the microscopic interference of wave packets in the R_3 Liouville pathway. However, the ground state dynamics observed in the SPE method results from a macroscopic interference. The experimental parameter that can be used to distinguish this macroscopic coherence is the distribution of the initial population, making the observation of this dynamics strongly dependent on the temperature. SPE is a powerful technique for studying intramolecular dynamics because it is not affected by inhomogeneous broadening. Using high-temperature samples it is possible to obtain molecular parameters such as vibrational relaxation and intramolecular vibrational redistribution of the ground electronic state through the macroscopic coherence. In this particular case, macroscopic interference is not a "deleterious" effect. In the following section we discuss other uses for macroscopic coherences.

5. Discussion

In this work, we calculated wave packet snapshots of processes occurring in rephasing (SPE) and nonrephasing (VE) signals observed in three-pulse FWM measurements. We identified microscopic

and macroscopic sources of interference. The theory was found to be in excellent agreement with the experimental data. The wave packet analysis of the nonlinear processes revealed three methods for controlling the observed third-order polarization. The first is based on preventing the interference between VE and SPE Liouville pathways. For noncollinear geometry and time-separated pulses, the SPE and VE contributions are easily separated because the two have different phase-matching directions that depend on the experimental geometry [13]. For FWM experiments with pairs of phase-locked collinear laser pulses, the four Liouville paths give interfering contributions to the signal [44–46]. The second control method uses the time delay between pulses to suppress or amplify a given Liouville path based on a pump–dump principle [19,21,27,28,34,47]. The amplitude modulation of the Liouville pathways is caused by the microscopic interference [13] and it gives rise to the well-known quantum beat phenomenon. Because FWM with phase-matched detection is a coherent nonlinear process, there is a third possibility to control the polarization involving macroscopic interference. For this case, superpositions of wave packets that belong to different molecules in the sample interfere. The FWM signal is a coherent superposition of signals generated through dipole coupling between wave packets from different initial vibrational levels in the ground state in different molecules. Ground state dynamics can thus be measured for setups like SPE where microscopic interference should only yield excited state dynamics. This process is identified as synchronization interference (see Fig. 8). Here we emphasize that this macroscopic interference within a homogeneous sample appears when multiple ground state levels are populated in the sample.

Macroscopic interference arises from different molecules, different pathways from one molecule, or different initial states in one Liouville pathway (as discussed in this paper). The experimental identification of macroscopic interference is not always straightforward. In this study, we show that nonlinear signals can be modulated by microscopic and macroscopic interference. It can therefore be assumed that in experiments where the observable is a nonlinear polarization, such as a Raman transition or the generation of high harmonics, macroscopic interference can play an important role. This may be the case in the experiments on coherent control of bond excitation from Ref. [48], as well as the work on shaped-pulse optimization of high harmonics from Ref. [49].

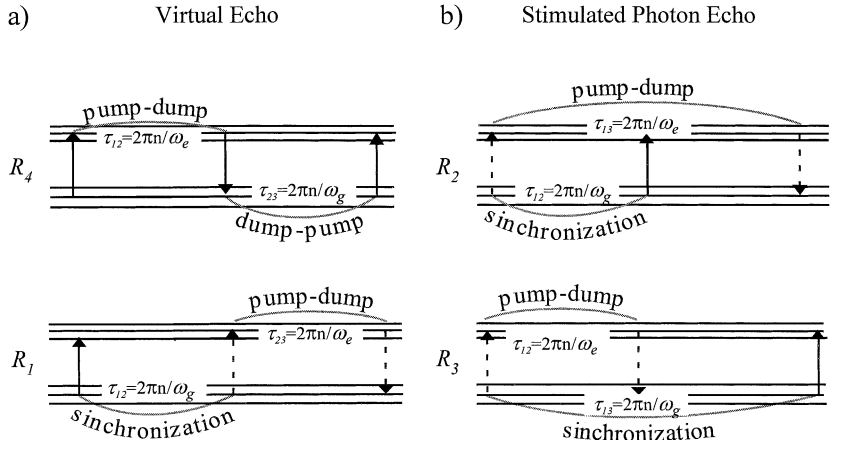

Fig. 8. Ladder diagrams for VE (R_4 and R_1) and for SPE (R_2 and R_3). The horizontal lines correspond to the vibrational states of the ground or excited states. The vertical arrows correspond to the absorption (up) or stimulated emission (down). The time goes from left to right. The solid lines correspond to transitions on the ket side, while the dashed lines to transitions on the bra. There are two control mechanisms. The first one, called "pump–dump", which is possible when sequential transitions take place on one side (bra or ket). The second mechanism, called "synchronization interference", is possible when there are two transitions from one electronic state to another on both (bra and ket) sides. Conditions for in-phase excitations, when signal is maximized are marked in the figures.

Clearly, macroscopic interference can help to modulate the observed signal. However, the role that macroscopic coherence can play in laser control of chemical reactions is not as clear.

We believe that optimal field control of chemical reactions takes advantage of both microscopic and macroscopic interference, especially for high-order nonlinear optical process, when there are many optical transitions between ground and excited states. If this premise is correct, then starting from a pure initial state using jet-cooled molecules can result in the loss of macroscopic interference and hence a loss of control 'knobs'. As shown in this study the presence of different initial states as in a chemical mixture or a thermal population can lead to modulation of the sample polarization. The overall polarization and not only the laser field can influence the outcome of a chemical process.

A large number of experiments have been carried out showing microscopic and macroscopic coherences. Our theoretical section provided a wave packet formalism to model FWM experiments with noncollinear pulses. Here we discuss other more familiar experimental setups. Consider the vibrational wave packet motion observed in molecular iodine following pump–probe measurements [50]. If the iodine molecules are initially in a pure state, then only microscopic coherence is observed. If more than one state is thermally populated then the initial excitation creates a number of microscopic coherences. The probe pulse interrogates the wave packets taking them to a new excited state and the signal corresponds to an incoherent sum of microscopic coherences.

Consider the experiment of Gerdy et al. on molecular iodine in the gas phase [51]. In that experiment two collinear pump pulses were used before the probe pulse. The observations were as follows. When the pump pulses were spaced by a time equal to an integer of the vibrational period of the excited state, $\tau_{12} = 2\pi n/\omega_e$, excited state oscillations were observed as a function of time delay of the probe pulse. When the pump pulses were spaced by a time equal to half of the vibrational period of the excited state, $\tau_{12} = 2\pi(n + 0.5)/\omega_e$, no oscillations were observed. The two wave packets formed in the excited state in this experiment have a well-defined phase and exhibit a macroscopic coherence. Unfortunately, the experiment by Gerdy was carried out without active phase stabilization between the two pump pulses. As the data was averaged to improve the signal to noise level, at each time delay with multiple laser shots and over multiple scans, the phase sensitive information was lost. Therefore, the results presented the incoherent sum of two pump–probe experiments. The experiments presented here on gas phase were obtained with similar laser pulses as used in Gerdy's experiment but phase coherence between the lasers was ensured by the phase-matching detection. The results obtained for the two time delays, $\tau_{12} = 2\pi n/\omega_e$ or $\tau_{12} = 2\pi(n + 0.5)/\omega_e$, are drastically different.

Experiments with two phase-locked pulses were carried out by Scherer et al. [52]. In these experiments, the first-order wave packets formed by each pulse interfere constructively or destructively in the first excited state depending on their relative phase. Scherer et al. detected the signal with lock-in amplification to get rid of the phase-insensitive signal and to enhance the phase-sensitive signal. The FWM signals from FWM experiments with phase-locked pulses have been analyzed by Cho et al. [12].

With two phase-locked pulses it is possible to observe photon echo emission as demonstrated by Warren and Zewail on gas phase iodine [53]. When three or more collinear pulses are phase locked, there is a possibility to observe microscopic as well as macroscopic coherences. The group of Wiersma has shown how the interference between different Liouville pathways, a macroscopic interference, leads to the cancellation of FWM signal [22,23]. It is reasonable to assume that experiments with shaped pulses, where the shaped pulse can be expressed as a combination of two or more phase-locked pulses, induce microscopic as well as macroscopic coherences that interfere. Therefore, a purely microscopic view of these experiments would miss the contribution of macroscopic coherences to the outcome.

In this article, we have chosen experiments with noncollinear phase-matched laser pulses to illustrate microscopic and macroscopic coherence phenomena. This setup ensures that the signal that is detected results from a phase-coherent

interaction of the three lasers. With noncollinear pulses it is easier to separate the different contributions to the signal and hence to separate macroscopic and microscopic coherence effects. We have also used a wave packet approach to model the observations and illustrate with snapshots every step of each Liouville pathway. The use of the density matrix formalism for calculating nonlinear optical signals is more efficient than the wave packet approach [13]. This is particularly true when relaxation processes are introduced. The wave packet approach allows one to distinguish between microscopic and macroscopic effects. Visualization of the nonlinear responses in terms of wave packet dynamics can be very valuable to understand these effects. Understanding the control possibilities for each of the Liouville path gives us the keys to analyze highly nonlinear effects introduced with intense and shaped laser pulses.

6. Conclusion

In this study, we have presented a wave packet representation for third-order processes indicating microscopic and macroscopic interference. Three sources of macroscopic interference are identified. The first is caused by interference between different Liouville pathways on different molecules. The second is caused by interference between the same Liouville pathway on different molecules. The third is caused by interference between different Liouville pathways from the same molecule. The theoretical formulation is used to model VE and SPE measurements on iodine vapor. The simulations were found to be in very good agreement with the data.

This paper is not limited in scope to three-pulse FWM with noncollinear pulses, the study provides an understanding that can be used to harness both microscopic and macroscopic interference for controlling quantum dynamics with lasers. These effects may act in tandem to control nonlinear optical effects such as high harmonics or Raman signals. For high-field interactions, macroscopic interference can also modulate the field that molecules experience thereby controlling the outcome of chemical processes.

Acknowledgements

It is a pleasure to acknowledge helpful discussions with Yi Jing Yan about the wave packet representation. We also thank Jeffrey Cina for providing us with a preprint of his work on wave packet interferometry. This research was partially funded by a grant from the National Science Foundation (CHE-9812584). MD is a Lucille and David Packard Science and Engineering Fellow, a Camille Dreyfus Teacher–Scholar, and an Alfred P. Sloan Fellow.

Appendix A

This model takes in to account vibrational and rotational motion and nuclear spin statistics. The results presented in this appendix correspond to a homonuclear diatomic molecule with two electronic resonance states, without vibrational relaxation and closely spaced rotational levels. All pulses must be spectrally degenerate, with a carrier frequency resonant with the electronic transition frequency (RWA must be valid), well separated in time, transform limited and with parallel linear polarization. The interaction of the molecule with the external field must be weak (first-order perturbation of each interaction). Homogeneous or inhomogeneous broadening as well as any initial coherence are neglected, a condition that is acceptable for modeling dynamics observed during the first few picoseconds on gas phase samples. The homodyne detected spectrally and time integrated signal intensity of SPE and VE measurements can be expressed as follows:

$$\begin{aligned} I^{\mathrm{SPE}}(t_1 = 0, t_2, t_3) &\propto \sum_{leg} \rho_l^2 \{ |B_{2eg}|^2 [6 + 4\cos(4\beta_e l t_3)] \\ &\quad + |B_{3eg}|^2 [6 + 4\cos(4\beta_e l t_2)] \\ &\quad + (B_{2eg} B_{3eg}^* + B_{2eg}^* B_{3eg}) [2 + 2\cos(4\beta_e l t_2) \\ &\quad + 2\cos(4\beta_e l t_3) + 2\cos(4\beta_e l (t_3 - t_2)) \\ &\quad + 2\cos(4\beta_g l (t_3 - t_2))] \}, \end{aligned} \tag{A.1}$$

$$
\begin{aligned}
I^{\mathrm{VE}}(t_1 = 0, t_2, t_3) &\propto \sum_{leg} \rho_l^2 \{ |B_{leg}|^2 [6 + 4\cos(4\beta_e l(t_3 - t_2))] \\
&\quad + |B_{4eg}|^2 [6 + 4\cos(4\beta_e l t_2) \\
&\quad + 4\cos(4\beta_g l(t_3 - t_2)) \\
&\quad + 4\cos(4\beta_e l t_2 + 4\beta_g l(t_3 - t_2))] \\
&\quad + (B_{1eg} B^*_{4eg} + B^*_{1eg} B_{4eg}) [2 + 2\cos(4\beta_e l t_2) \\
&\quad + 2\cos(4\beta_e l t_3) + 2\cos(4\beta_e l(t_3 - t_2)) \\
&\quad + 2\cos(4\beta_g l(t_3 - t_2)) \\
&\quad + 2\cos(4(\beta_e - \beta_g) l(t_3 - t_2))] \}, \qquad \text{(A.2)}
\end{aligned}
$$

where e and g vibrational quantum numbers in electronically excited and ground states; l is the rotational quantum number and the other parameters are defined below.

Vibrational dynamics through Liouville pathways R_1–R_4:

$$
\begin{aligned}
B_{1eg} &= \mu_{eg} \sum_{e'g'} \rho_{g'} \exp(\mathrm{i}(\Omega_{e'} - \Omega_g) t_3) \\
&\quad \times \exp(\mathrm{i}(\Omega_{g'} - \Omega_{e'}) t_2) A^{[3]}_{e'g} A^{[2]}_{e'g'} A^{[1]}_{eg'}, \\
B_{2eg} &= \mu_{eg} \sum_{e'g'} \rho_{g'} \exp(\mathrm{i}(\Omega_{e'} - \Omega_g) t_3) \\
&\quad \times \exp(\mathrm{i}(\Omega_e - \Omega_{g'}) t_2) A^{[3]}_{e'g} A^{[2]}_{eg'} A^{[1]}_{e'g'}, \\
B_{3eg} &= \mu_{eg} \sum_{e'g'} \rho_{g'} \exp(\mathrm{i}(\Omega_e - \Omega_{g'}) t_3) \\
&\quad \times \exp(\mathrm{i}(\Omega_{e'} - \Omega_g) t_2) A^{[3]}_{eg'} A^{[2]}_{e'g} A^{[1]}_{e'g'}, \\
B_{4eg} &= \mu_{eg} \sum_{e'g'} \rho_g \exp(\mathrm{i}(\Omega_e - \Omega_{g'}) t_3) \\
&\quad \times \exp(\mathrm{i}(\Omega_{g'} - \Omega_{e'}) t_2) A^{[3]}_{eg'} A^{[2]}_{e'g} A^{[1]}_{e'g}. \qquad \text{(A.3)}
\end{aligned}
$$

$A^{[n]}_{eg}$ is the spectral amplitude of interaction with nth pulse,

$$
A^{[n]}_{eg} = 2\frac{\mu_{eg}}{\hbar}\sqrt{S^{[n]}_{eg}}, \qquad \mu_{eg} = \mu\sqrt{\mathrm{CFC}_{eg}}, \qquad \text{(A.4)}
$$

where $S^{[n]}_{eg}$ and CFC_{eg} are power spectra of the nth pulse and the Frank Condon coefficients for the frequencies of the $e \leftarrow g$ vibrational transitions; μ is the electronic dipole moment. The vibrational frequencies are

$$
\Omega_e = \varepsilon_e/\hbar - \omega_0, \qquad \Omega_g = \varepsilon_g/\hbar, \qquad \text{(A.5)}
$$

where ε_e and ε_g are the energy levels in excited e and ground g states and ω_0 is the current frequency of the spectrally degenerate pulses. The expression for β_g and β_e are given by the rotational constants in ground B_g and excited B_e states,

$$
\beta_g = 2\pi B_g c, \qquad \beta_e = 2\pi B_e c. \qquad \text{(A.6)}
$$

ρ_g corresponds to the initial population of the g vibrational state in ground electron state,

$$
\begin{aligned}
\rho_g &= Q_v^{-1} \exp(-\varepsilon_g/kT), \quad Q_v \\
&= \sum_g \exp(-\varepsilon_g/kT). \qquad \text{(A.7)}
\end{aligned}
$$

ρ_l is the initial population in state with angular momentum l is

$$
\begin{aligned}
\rho_l &= Q_r^{-1}(2l+1) g_l \exp[-\beta_g h l(l+1)/kT], \\
Q_r &= \sum_l (2l+1) g_l \exp[-\beta_g h l(l+1)/kT], \qquad \text{(A.8)}
\end{aligned}
$$

where g_l is the statistical weight for symmetrical $\Sigma_{+\mathrm{g}}$ ground electronic state and is given by

$$
g_l \propto \left\{ \begin{array}{ll} I+1 & (\text{odd } l) \\ I & (\text{even } l) \end{array} \right\} \text{ when nuclei are fermions,}
\quad
\left\{ \begin{array}{ll} I & (\text{odd } l) \\ I+1 & (\text{even } l) \end{array} \right\} \text{ when nuclei are bosons,} \qquad \text{(A.9)}
$$

where I is nuclear spin.

References

[1] D.J. Tannor, R. Kosloff, S.A. Rice, J. Chem. Phys. 85 (1986) 5805.
[2] D.J. Tannor, S.A. Rice, Adv. Chem. Phys. 70 (1988) 441.
[3] P. Brumer, M. Shapiro, Annu. Rev. Phys. Chem. 43 (1992) 257.
[4] R.M. Bowman, M. Dantus, A.H. Zewail, Chem. Phys. Lett. 174 (1990) 546.
[5] T. Baumert, G. Gerber, Isr. J. Chem. 34 (1994) 103.
[6] T. Baumert, R. Thalweiser, V. Weiss, G. Gerber, Femtosecond time-resolved photochemistry of molecules and metal clusters, in: J. Manz, L. Wöste (Eds.), Femtosecond Chemistry, VCH, Weinheim, 1995, p. 397.
[7] A. Assion, T. Baumert, J. Helbing, V. Seyfried, G. Gerber, Chem. Phys. Lett. 259 (1996) 488.
[8] I.S. Averbukh, M.J.J. Vrakking, D.M. Villeneuve, A. Stolow, Phys. Rev. Lett. 77 (1996) 3518.

[9] L.O. Lambert, A. Compaan, I.D. Abella, Phys. Rev. A 4 (1972) 2022.
[10] W.B. Mims, Phys. Rev. B 6 (1972) 3543.
[11] Y.J. Yan, S. Mukamel, J. Chem. Phys. 94 (1991) 179.
[12] M. Cho, N.F. Sherer, G.G. Fleming, S. Mukamel, J. Chem. Phys. 96 (1992) 5618.
[13] S. Mukamel, Principles of Nonlinear Optical Spectroscopy, Oxford University Press, New York, 1995.
[14] R. Leonhardt, W. Holzapfel, W. Zinth, W. Kaizer, Chem. Phys. Lett. 133 (1987) 373.
[15] T.H. Joo, M.A. Dugan, A.C. Albrecht, Chem. Phys. Lett. 177 (1991) 4.
[16] O. Rubner, M. Schmitt, G. Knopp, A. Materny, W. Kiefer, V. Engel, J. Phys. Chem. A 102 (1998) 9734.
[17] M. Koch, J. Feldman, G. von Plessen, E.O. Göbel, P. Thomas, K. Köhler, Phys. Rev. Lett. 69 (1992) 3631.
[18] R.W. Schoenlein, D.M. Mittleman, J.J. Shiang, A.P. Alivisatos, C.V. Shank, Phys. Rev. Lett. 70 (1993) 1014.
[19] C.J. Bardeen, C.V. Shank, Chem. Phys. Lett. 203 (1993) 535.
[20] T.H. Joo, A.C. Albrecht, Chem. Phys. 173 (1993) 17.
[21] C.J. Bardeen, C.V. Shank, Chem. Phys. Lett. 226 (1994) 310.
[22] W.P. de Boeij, M.S. Pshenichnikov, D.A. Wiersma, J. Chem. Phys. 105 (1996) 2953.
[23] W.P. de Boeij, M.S. Pshenichnikov, D.A. Wiersma, Chem. Phys. 233 (1998) 287.
[24] Y.R. Shen, The Principle of Nonlinear Optics, Wiley, New York, 1984.
[25] D. Lee, A.C. Albrecht, A unified view of Raman, resonance Raman, and fluorescence spectroscopy (and their analogues in two-photon absorption), in: R.J.H. Clark, R.E. Hester (Eds.), Advances in Infrared and Raman Spectroscopy, vol. 12, Wiley-Heyden, Chichester, 1985.
[26] R.W. Boyd, Nonlinear Optics, Academic Press, San Diego, 1992.
[27] I. Pastirk, E.J. Brown, B.I. Grimberg, V.V. Lozovoy, M. Dantus, Faraday Discuss. 113 (1999) 401.
[28] V.V. Lozovoy, I. Pastirk, E.J. Brown, B.I. Grimberg, M. Dantus, Int. Rev. Phys. Chem. 19 (2000) 531.
[29] B.I. Grimberg, V.V. Lozovoy, M. Dantus, S. Mukamel, J. Phys. Chem., submitted (2001).
[30] J. Tellinghuisen, J. Quant. Spectrosc. Radiat. Transf. 19 (1978) 149.
[31] S. Gerstenkorn, P. Luc, J. Physique 46 (1985) 867.
[32] M. Motzkus, S. Pedersen, A.H. Zewail, J. Phys. Chem. 100 (1996) 5620.
[33] E.J. Brown, Q. Zhang, M. Dantus, J. Chem. Phys. 110 (1999) 5772.
[34] I. Pastirk, V.V. Lozovoy, B.I. Grimberg, E.J. Brown, M. Dantus, J. Phys. Chem. A 103 (1999) 10226.
[35] M. Schmitt, G. Knopp, A. Materny, W. Kiefer, Chem. Phys. Lett. 280 (1997) 339.
[36] S. Meyer, M. Schmitt, A. Materny, W. Kiefer, V. Engel, Chem. Phys. Lett. 301 (1999) 248.
[37] T. Chen, V. Engel, M. Heid, W. Kiefer, G. Knopp, A. Materny, S. Meyer, R. Pausch, M. Schmitt, H. Schwoerer, T. Siebert, J. Mol. Struct. 481 (1999) 33.
[38] S. Meyer, V. Engel, J. Raman. Spectrosc. 31 (2000) 33.
[39] S. Meyer, V. Engel, Appl. Phys. B 71 (2000) 293.
[40] A. Materny, T. Chen, M. Schmitt, T. Siebert, A. Vierheilig, V. Engel, W. Kiefer, Appl. Phys. B 71 (2000) 299.
[41] Y. Prior, Appl. Opt. 19 (1980) 1741.
[42] J.A. Shirley, R.J. Hall, A.C. Eckbreth, Opt. Lett. 5 (1980) 380.
[43] E.J. Brown, I. Pastirk, B.I. Grimberg, V.V. Lozovoy, M. Dantus, J. Chem. Phys. 111 (1999) 3779.
[44] N.F. Scherer, A.J. Ruggiero, M. Du, G.R. Fleming, J. Chem. Phys. 93 (1990) 856.
[45] N.F. Scherer, R.J. Carlson, A. Matro, M. Du, A.J. Ruggiero, V. Romerorochin, J.A. Cina, G.R. Fleming, S.A. Rice, J. Chem. Phys. 95 (1991) 1487.
[46] J.A. Cina, J. Chem. Phys. 113 (2000) 9488.
[47] V.V. Lozovoy, B.I. Grimberg, E.J. Brown, I. Pastirk, M. Dantus, J. Raman Spectrosc. 31 (2000) 41.
[48] T.C. Weinacht, J.L. White, P.H. Bucksbaum, J. Phys. Chem. A 103 (1999) 10166.
[49] R. Bartels, S. Backus, E. Zeek, L. Misoguti, G. Vdovin, I.P. Christov, M.M. Murnane, H.C. Kapteyn, Nature 406 (2000) 164.
[50] M. Dantus, R.M. Bowman, A.H. Zewail, Nature 343 (1990) 737.
[51] J.J. Gerdy, M. Dantus, R.M. Bowman, A.H. Zewail, Chem. Phys. Lett. 171 (1990) 1.
[52] N.F. Scherer, A. Matro, L.D. Ziegler, M. Du, J. Carlson, J.A. Cina, G.R. Fleming, J. Chem. Phys. 96 (1992) 4180.
[53] W.S. Warren, A.H. Zewail, Laser Chem. 2 (1983) 37.